Ultrafast electron cycloids driven by the transverse spin of a surface acoustic wave

Maximilian M. Sonner, Farhad Khosravi, Lisa Janker, Daniel Rudolph, Gregor Koblmüller, Zubin Jacob, Hubert J. Krenner

Angaben zur Veröffentlichung / Publication details:

Sonner, Maximilian M., Farhad Khosravi, Lisa Janker, Daniel Rudolph, Gregor Koblmüller, Zubin Jacob, and Hubert J. Krenner. 2021. "Ultrafast electron cycloids driven by the transverse spin of a surface acoustic wave." *Science Advances* 7 (31): eabf7414. https://doi.org/10.1126/sciadv.abf7414.

PHYSICS

Ultrafast electron cycloids driven by the transverse spin of a surface acoustic wave

Maximilian M. Sonner[1†], Farhad Khosravi[2,3†], Lisa Janker[1†], Daniel Rudolph[4], Gregor Koblmüller[4], Zubin Jacob[3]*, Hubert J. Krenner[5,1]*

Spin-momentum locking is a universal wave phenomenon promising for applications in electronics and photonics. In acoustics, Lord Rayleigh showed that surface acoustic waves exhibit a characteristic elliptical particle motion strikingly similar to spin-momentum locking. Although these waves have become one of the few phononic technologies of industrial relevance, the observation of their transverse spin remained an open challenge. Here, we observe the full spin dynamics by detecting ultrafast electron cycloids driven by the gyrating electric field produced by a surface acoustic wave propagating on a slab of lithium niobate. A tubular quantum well wrapped around a nanowire serves as an ultrafast sensor tracking the full cyclic motion of electrons. Our acousto-optoelectrical approach opens previously unknown directions in the merged fields of nanoacoustics, nanophotonics, and nanoelectronics for future exploration.

INTRODUCTION

In 1885, Lord Rayleigh investigated wave propagation on the surface of an elastic medium. He recognized that one specific mode, the "rolling" Rayleigh mode, exhibits a characteristic counterclockwise elliptical motion in the plane normal to the surface and parallel to the propagation (*1*). This gyrating motion corresponds to an angular momentum that is remarkably similar to spin-momentum locking, a universal property observed in electromagnetic (*2*–*11*) as well as electronic (*12*–*14*) systems where the momentum of the waves, the decay direction, and the spin form a locked triplet (see Fig. 1A). In photonics, this directional transport of energy, dependent on local polarization of evanescent waves, has been observed in quantum dot emission near topological photonic crystals (*15*–*17*), scattering of surface plasmon polaritons in metasurfaces (*3*, *18*), and cold atoms coupled to an optical fiber (*4*). Moreover, in 2D materials, recent experiments demonstrated that the coupling between the valley pseudospin of tungsten disulfide (WS_2) and the optical spin of plasmons in a silver nanowire (NW) results in the directional propagation of circularly polarized excitations (*19*). A similar phenomenon has also been observed in magnon modes of a spherical yttrium iron garnet magnon resonator where the spin-orbit coupling in the whispering gallery modes leads to a strong nonreciprocity (*20*). Recent work has also shown that electrons passing through chiral molecules exhibit spin selectivity in the transmission (*21*, *22*). This opens the intriguing question of observing spin-momentum locking and related phenomena in acoustic waves.

Acoustic waves, described by the motion of mechanical degrees of freedom, are fundamentally different compared to the electromagnetic modes in photonics and fermionic states in electronics. However, spin-momentum locking is a universal phenomenon arising from evanescent waves, and therefore, striking parallels exist between electromagnetic, electronic, and acoustic waves (*23*–*26*). More specifically, Rayleigh surface acoustic waves (SAWs) (*1*) exhibit both transverse and longitudinal displacement, with respect to the propagation direction on the surface of a material, with an intrinsic phase difference between these two components. Analogous to surface plasmon polaritons, the manifestation of acoustic spin in Rayleigh SAWs makes them an archetypical example of spin-momentum locking for elastic waves. These SAWs have the potential to be integrated on-chip alongside photonic and electronic technologies. They also find a myriad of applications ranging from quantum technologies for information transduction between microwave and optical frequencies to the life sciences (*27*). Despite the fact that Lord Rayleigh postulated the existence of a gyrating, elliptical motion, the direct observation of this transverse spin angular momentum has remained an open challenge.

The observation of the spin of Rayleigh SAW is challenging and requires a vector field sensor functioning at megahertz to gigahertz frequencies. It should be noted that conventional methods of detecting acoustic spin of airborne sound at lower audible frequencies up to a few kilohertz exploit macroscopic meta-atoms with dimensions in the millimeter to centimeter scale. Consequently, these macroscopic dimensions and moderate periods do not demand advanced detection schemes. Hence, macroscopic pressure sensors can be directly used to sense the local pressure field and, thus, acoustic spin of airborne sound (*28*, *29*). In strong contrast, these methods cannot be applied to detect the spin of a radio frequency (rf) Rayleigh SAW at $\geq$100 MHz because the approximately one order of magnitude higher phase velocity shrinks the wavelength to a few micrometers. Here, we use piezoelectric materials as the substrate for the propagation of Rayleigh SAWs because they produce a gyrating electric field, resulting from the SAW, on the surface of the piezoelectric material (*30*, *31*). Direct observation of this spinning field, however, requires an ultrafast sensor at the nanoscale specifically sensitive to electric fields. Existing nanoscale field probes such as nitrogen-vacancy centers in diamond only respond to the magnetic field and also average over the temporal signal for the observation of the field. We therefore use semiconductor NWs to

[1]Lehrstuhl für Experimentalphysik 1, Institut für Physik, Universität Augsburg, Universitätsstraße 1, 86159 Augsburg, Germany. [2]Department of Electrical and Computer Engineering, University of Alberta, Edmonton, Alberta T6G 1H9, Canada. [3]Birck Nanotechnology Center, School of Electrical and Computer Engineering, Purdue University, West Lafayette, IN 47906, USA. [4]Walter Schottky Institut and Physik Department E24, Technische Universität München, Am Coulombwall 4, 85748 Garching, Germany. [5]Physikalisches Institut, Westfälische Wilhelms-Universität Münster, Wilhelm-Klemm-Straße 10, 48149 Münster, Germany.
*Corresponding author. Email: krenner@wwu.de (H.J.K.); zjacob@purdue.edu (Z.J.)
†These authors contributed equally to this work.

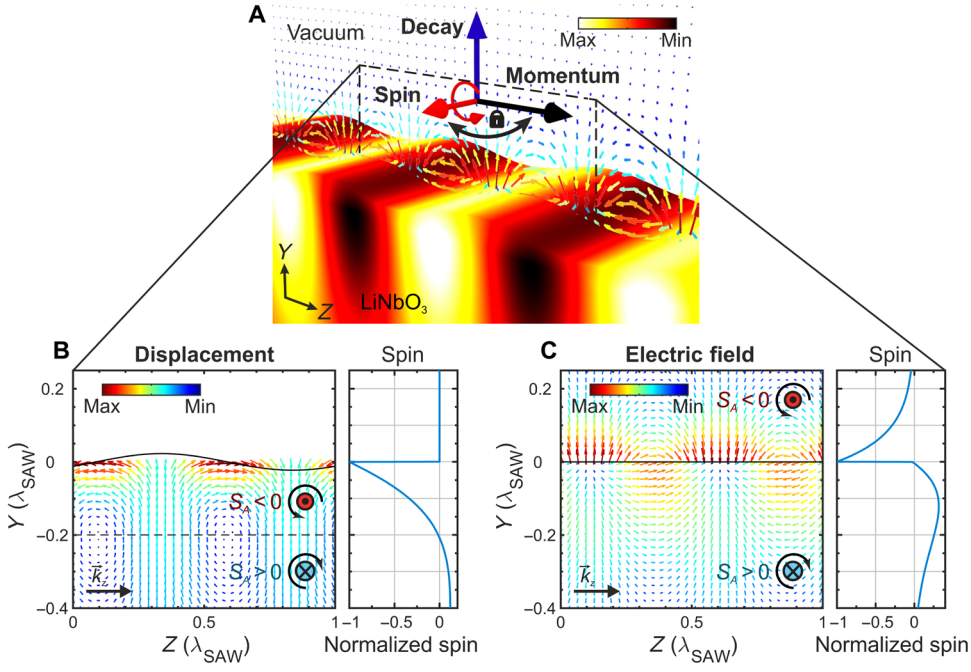

Fig. 1. Spin-momentum locking of a Rayleigh SAW. (**A**) Calculated real-space profile of a Rayleigh SAW propagating along the *z* direction on a *Y*-cut $LiNbO_3$ crystal. The color code is the piezoelectric potential, and arrows show the calculated electric field in the half-space above the solid. Momentum, decay, and spin of the gyrating electric field generated by a Rayleigh-type SAW form a right-handed triplet. The direction of spin for both electric field and displacement is locked to the propagation direction. Calculated displacement (**B**) and electric field (**C**) (main panels) of the Rayleigh SAW. The side panels show the normalized magnitude of the transverse spin normal to the surface ($Y = 0$) calculated from the mechanical motion and electric field as described in the main text. The mechanical spin shows a characteristic sign change at $\approx 0.2 \times \lambda_{SAW}$ below the surface, i.e., from being counterclockwise to clockwise, while the electrical spin changes from counterclockwise to clockwise exactly at the surface.

propose a unique spin sensor for the direct temporal observation of this gyrating electric field (*32*, *33*).

In this paper, we directly observe the spin of the electric field produced as a result of a Rayleigh SAW propagating on the surface of a lithium niobate ($LiNbO_3$) slab, a versatile piezoelectric material (*34*) with nonlinear and on-chip applications, merging the fields of nanophotonics and nanoacoustics (*35*–*37*). In our work, this spin is the angular momentum of a classical wave rather than a quantum mechanical Fock state (*38*). We exploit a unique NW sensor with a tubular quantum well (QW) that provides a direct signature of spin-momentum locking in acoustic waves through time-resolved motion of electron cycloids. Our approach maps the entire gyrating vector field, within a subwavelength volume, through a time-resolved probe of the longitudinal and transverse motion of charges in the NW sensor. It is fundamentally different from methods used in photonics and electronics, where the consequences of the spin-momentum locking are inferred only indirectly through the directionality of the propagating fields. Our NW sensor is a unique metrology tool for the observation of vector electric field oscillations at the nanoscale with ultrafast temporal resolution.

RESULTS

Equations of motions for the surface electric and acoustic waves on the surface of a piezoelectric material are solved numerically for one of the technologically most relevant SAW substrates, $LiNbO_3$ (*30*, *31*). We consider, with no loss of generality, that the Rayleigh SAW is propagating along the *Z* direction of a *Y*-cut $LiNbO_3$ crystal. Figure 1A shows the calculated real-space profile of the SAW with the color-coded electric potential superimposed. Figure 1 (B and C) shows the displacement and the electric fields in the sagittal plane marked in Fig. 1A. The electromagnetic and acoustic spin are given by $S_E = \frac{1}{2\omega}\mathrm{Im}(\epsilon_0 E^* \times E + \mu_0 H^* \times H)$ (*39*–*41*) and $S_A = \frac{1}{2\omega}\mathrm{Im}(\rho v^* \times v)$ (*24*, *28*), respectively, where *E*, *H*, ρ, and *v* are the electric field, magnetic field, mass density, and velocity vector, respectively. In solving the equations for the Rayleigh waves, the electrostatic approximation has been assumed. Therefore, the contribution to the electromagnetic spin S_E comes only from the electric field in our case. The side panels of Fig. 1 (B and C) show the normalized acoustic and electromagnetic fields as a function of *Y* coordinate for propagation along positive *Z* direction ($k_Z > 0$). The acoustic spin analyzed in the side panel of Fig. 1B is pointing out of the sagittal plane close to the interface, and it flips the sign at about 0.2 wavelength away from the interface as shown by the dashed line. This shows that although the direction of acoustic spin is locked to the direction of momentum, it does not necessarily form a conventional right-handed triplet with the momentum and decay, which is a property specific to Rayleigh-type SAWs. For the electromagnetic spin, however, as shown in the side panel of Fig. 1C, the spin is pointing out of the plane on top of the surface. Therefore, the momentum, decay, and spin form a right-handed triplet as indicated in Fig. 1A. Inside the material, the electromagnetic spin flips together with the decay direction. Thus, the right-hand momentum, decay, and spin triplet are preserved.

Next, we demonstrate the direct experimental observation of the electric spin of the SAW (Fig. 2A). We fabricated a SAW device comprising an interdigital transducer (IDT) that enables the electromechanical excitation of a SAW propagating with a phase velocity c_{SAW} = 3495 m/s by applying an rf voltage matched to the IDT

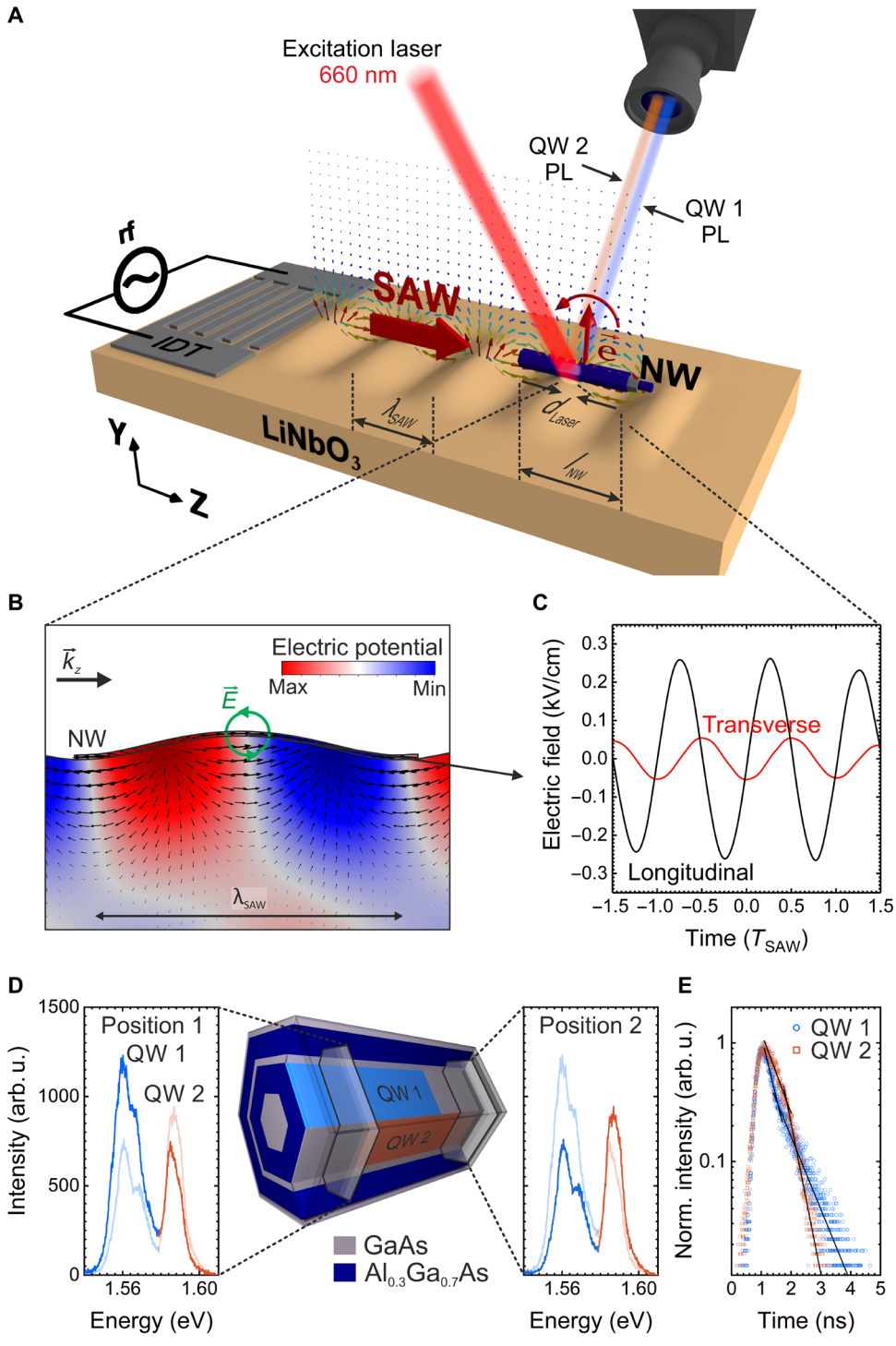

Fig. 2. Experimental setup. (**A**) Schematic of device comprising a $LiNbO_3$ substrate and the sensor NW (not to scale) placed on its surface. The SAW is generated by applying an ac voltage to an IDT, and the orientation of the NW is chosen to be along the propagation direction of the SAW. A pulsed laser is focused to a d_{Laser} = 1.5-μm-diameter spot and excites carriers in the NW at a well-defined time during the acoustic cycle. The emission of the two QW segments is spectrally filtered and detected. (**B**) Calculated electric potential of the SAW in the $LiNbO_3$ substrate and the NW. (**C**) Longitudinal and transverse components of $\vec{E}$ in the center of the NW showing the π/2-phase shift characteristic for Rayleigh SAWs. (**D**) Schematic of the tubular QW heterostructure wrapped around the core of the NW. QW1 (blue) and QW2 (red) are offset by $d_{axial} \approx$ 2.0 μm along the axis of the NW and located on the upper- and lower-side facet, respectively. The PL spectra from two positions show that the QW1 and QW2 can be distinguished by their characteristic emission energies. arb. u., arbitrary units. (**E**) The time-dependent PL emissions of QW1 and QW2 show clear anticorrelation, proving that both localization sites are interconnected.

design. Further details can be found in the Supplementary Materials. The design wavelength of λ_{SAW} = 18 μm of the IDT corresponds to a precession period of SAW's spin of T_{SAW} = 5.150 ns. Experiments are performed at a temperature of T = 8 K. Thus, the thermal energy exceeds the energy of a single phonon ($k_BT \gg h/T_{SAW}$), placing our experiment in the classical multiphonon regime. A single semiconductor NW is transferred onto the surface of a conventional SAW chip, and electrons inside this nanostructure couple strongly to the electrical spin of the SAW. Figure 2 (B and C) shows the result of finite element modeling confirming strong electrical coupling of the SAW propagating on the surface of $LiNbO_3$ to the semiconductor NW. Here, we consider an NW whose length is set to λ_{SAW} to sample all local phases of the SAW in a single simulation run (*42*). The spatial profile of the electric potential (color-coded) is presented in Fig. 2B together with the derived electric field (arrows). The SAW's electrical component is directly transferred into the NW. This is further corroborated in Fig. 2C, in which the time evolutions of the transverse (normal to the surface) and longitudinal (parallel to the propagation direction) electric field components are evaluated at a fixed position in the NW. These simulation data confirm that the characteristic π/2 phase shift between the longitudinal and transverse electric field components of the SAW on $LiNbO_3$ is faithfully preserved inside the NW.

The NW sensor itself contains a hexagonal cross-sectional GaAs/(Al)GaAs multishell heterostructure, wrapped around its l_{NW} = 10-μm-long GaAs core. The schematic in Fig. 2D shows that a nominally 5-nm GaAs (gray) tubular QW is sandwiched in higher bandgap $Al_{0.3}Ga_{0.7}As$ barriers. Further details on the NW growth can be found in the Supplementary Materials and in (*33*). The unique three-dimensional nature of this heterostructure is key for the experimental observation of the transverse spin of the SAW. During growth of this radial heterostructure, thickness fluctuations and deviation from a perfect hexagonal cross section occur (*33*), which is crucial for our ultrafast nanoscale sensing experiment. For this particular NW, the thickness of the QW is locally increased compared to its nominal value in two distinct segments highlighted in red and blue in Fig. 2D. In the following, we refer to these segments as QW1 (blue) and QW2 (red), respectively. In each segment, the electron energy wave function localizes, which leads to a reduction of the quantization energies, and the two segments can be readily distinguished from their optical emission. QW1 and QW2 are spatially displaced.

The two interconnected segments QW1 and QW2 are offset both along the propagation direction of the SAW and in its transverse direction normal to the $LiNbO_3$ surface. This offset is crucial for the isolation of signatures corresponding to transverse spin of the SAW. Therefore, we present extensive evidence characterizing the fundamental behavior of the NW sensor. Figure 2D shows photoluminescence (PL) spectra recorded from two positions in the left and center panels. The spectrum from the other position is plotted in light lines in each panel for comparison. The two positions are offset along the NW axis by $d_{axial} \approx 2.0$ μm. The detected PL signal stems from recombination of electrons and holes generated by a 660-nm laser within the radial QW. At position 1 (left), emission of QW1 (blue) at an energy of about 1.562 eV dominates, while emission of QW2 (red) at an energy of about 1.585 eV is comparably weak. When moving to position 2 (center), precisely the opposite intensity distribution is observed, with QW2 showing a higher intensity compared to QW1. These observations prove that the two segments are offset along the axis of the NW, with QW1 being closer to the IDT launching the SAW. Furthermore, QW1 and QW2 are located on different side facets of the hexagon, with QW1 being on the upper facet, while QW2 is located on the lower facet closer to the $LiNbO_3$ surface. Moreover, the fact that both emission peaks are observed at both positions is a first indication that the two regions are interconnected and carriers can be exchanged between them.

We now present time-resolved PL experiments that characterize the NW sensor behavior without the presence of the exciting SAW. The detected time transients of QW1 and QW2 are compared in Fig. 2E. We observe coupled emission dynamics of QW1 and QW2: While QW1 exhibits a fast decay (time constant $\tau_{QW1,fast}$ = 0.4 ns) at short times and a slow time constant ($\tau_{QW1,slow}$ = 0.7 ns) at longer times, the behavior of QW2 is exactly opposite with $\tau_{QW2,fast}$ = 0.3 ns and $\tau_{QW2,slow}$ = 0.6 ns, respectively. These anticorrelated recombination rates are an unambiguous fingerprint of coupled emission dynamics and, thus, direct evidence that QW1 and QW2 are interconnected. We will exploit these coupled charge carrier dynamics of QW1 and QW2 to isolate the temporal signature of gyrating electric fields.

In our experiment to probe spin for the SAW, we define an absolute time (t): This time is set by the sinusoidal oscillation of the SAW's transverse displacement component, u_Y, which is plotted in blue in the center as shown in Fig. 3A. At t = 0, the electric field vector $\vec{E}$ is transverse, pointing downward toward the substrate. As shown in the top panel, $\vec{E}$ (red arrow) undergoes its characteristic counterclockwise gyration at the position of QW1 and QW2 with a period of T_{SAW} = 5.15 ns. Furthermore, we excite the NW by a $\tau_{Laser} \simeq$ 0.09-ns-long laser pulse shown in red in Fig. 3A. The delay between the laser pulse and the absolute time set by the SAW is denoted as τ. Thus, the laser pulse generates electrons and holes in the QW at a well-defined time during the acoustic cycle. The time-dependent electric field couples to charge carriers inside the three-dimensional heterostructure of the NW via the acoustoelectric effect. The transport mobility of electrons is approximately one order of magnitude greater than that of holes (*43*). Thus, at the SAW power (P_{rf} = −4 dBm) applied in our experiments, the photogenerated holes remain quasi-stationary. We can attribute our experimental observation faithfully to spatiotemporal dynamics of electrons (*32*). This coupling enables us to observe the transverse spin of the SAW and is illustrated schematically in Fig. 3B. In these schematics, the directions along which the electric field $\vec{E}$ accelerates electrons (black) inside the heterostructure at distinct absolute times are indicated by the green arrows. For instance, at t = 0 (schematic I), $\vec{E}$ is oriented along the $-Y$ direction, pointing toward the substrate. Thus, electrons are accelerated upward in the opposite direction inside the heterostructure. As t progresses, $\vec{E}$ gyrates counterclockwise. The negative charge of the electron does not affect the counterclockwise sense of this gyration, which is fully preserved. However, the direction of the accelerating force exhibits a π phase shift that can be directly seen in the sequence of schematics I to IV.

Figure 3 (C and D) shows experimental data evidencing the cyclic motion of the electrons driven by the SAW's transverse angular momentum for an exemplary delay $\tau = -\frac{T_{SAW}}{6}$. The raw PL time transients of QW1 (blue) and the other one of QW2 (red) are plotted in Fig. 3C. We process these data and determine the degree of normalized emission intensity defined as DoEI = $\frac{I_{QW1} - I_{QW2}}{I_{QW1} + I_{QW2}}$. This quantity is a measure of the electron population of the two QW segments, with DoEI = +1 and DoEI = −1 for emission occurring only from QW1 and QW2, respectively. In the Supplementary Materials, we present additional data in which we tune τ over a full acoustic

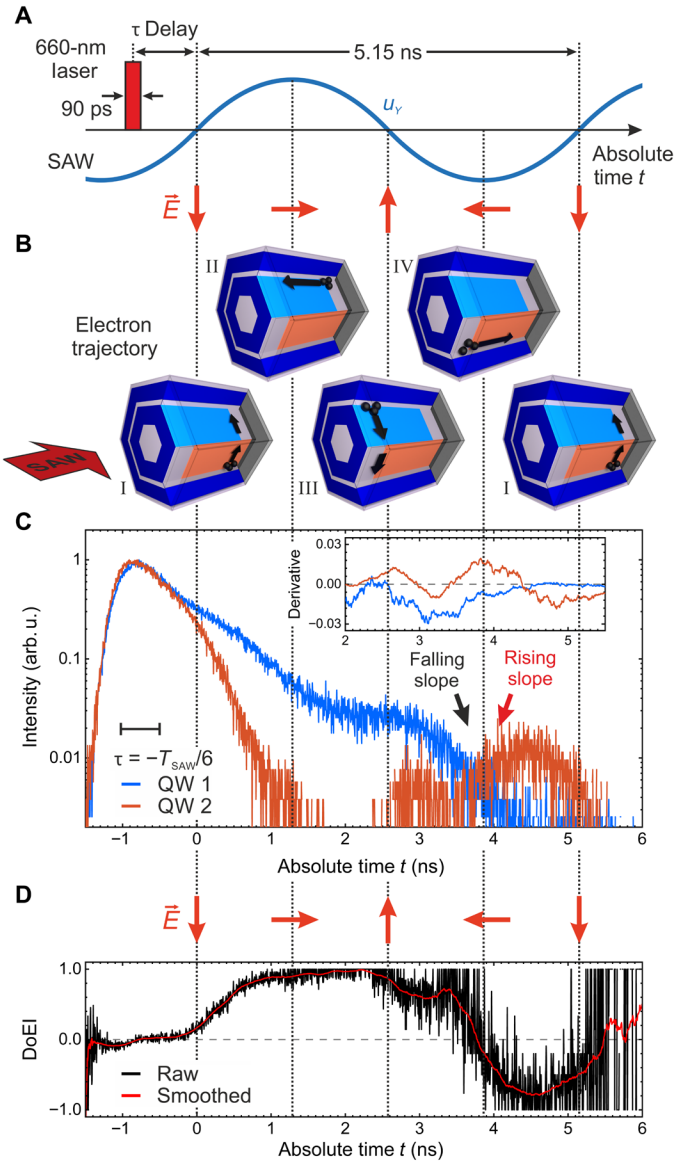

Fig. 3. Observation of the SAW's transverse spin. (**A**) The transverse displacement component u_Y (blue) oscillates with the SAW's period of T_{SAW} = 5.15 ns. Electrons and holes are injected by photoexcitation using a pulsed laser, marked in red, at a freely programmable delay τ during the acoustic cycle. As time progresses, the electric field vector gyrates as indicated in the lower part. (**B**) The schematics show the motion of electrons (black) within the QW at distinct times during the acoustic cycle. The direction of this motion is exactly opposite to the orientation of $\vec{E}$ and leads to cyclic, gyrating trajectories. The sense of this cycloid is set by the transverse spin. (**C**) Experimental observation of electron cycloids in the time-dependent PL of QW1 (blue) and QW2 (red). The two transients exhibit clear anticorrelated rising and falling slopes (arrows) at characteristic times during the acoustic cycles shown in (B). These anticorrelations are direct evidence for the cyclic motion of the electrons inside the tubular QW. The inset shows the transients illustrating the opposite slopes of the two signals in the selected time interval. A conservative estimate of the temporal resolution is given by the scale bar. (**D**) Degree of normalized emission intensity DoEI $= \frac{I_{QW1} - I_{QW2}}{I_{QW1} + I_{QW2}}$ derived from the data in (C). The black and red lines are raw and smooth data, respectively.

cycle and, thus, map out the full dynamics. These data corroborate the observation of the transverse acoustic spin of the SAW. The schematics show that the direction electrons (black) are accelerated in the region of QW1 and QW2 as the absolute time t progresses. For $t = 0$, the electric field is pointing downward along $-Z$ (schematic I) and, thus, electrons are accelerated in the opposite direction toward the upper facet of the NW. In the raw time transients in Fig. 3C, we observe a quenching of the emission intensity of QW2, while that of QW1 remains high. This anticorrelated nature can be clearly seen as an increase of the DoEI in Fig. 3D, which is direct evidence of coupled depopulation of QW2 and population of QW1. The electrons are accelerated from the lower to upper facet due to the transverse component of the electric field because the segments are located at different side facets as indicated in the schematics. As t progresses, the intensity of QW2 remains low, while that of QW1 decays very slowly, leading to a plateau of DoEI. These observations arise due to the combination of two effects: the injection of electrons into the region of QW1 and the depopulation of QW2. This first effect is induced by the electric field being parallel to the wave vector of the SAW $\vec{E} \parallel \vec{k}$, accelerating electrons in the opposite direction as shown in schematic II. The next distinct effect occurs during the acoustic cycle at t = 2.7 ns. At this time, $\vec{E}$ is transverse, pointing upward, and consequently, electrons are moving toward the substrate. This leads to a depopulation of the upper facet on which QW1 is located and an injection into QW2 on the lower facet. As time progresses, the electric field vector rotates, and electrons are accelerated along the axial direction toward QW2. In the experimental data, we observe precisely the expected anticorrelated behavior of the emission of QW1 quenching that of QW2 reappearing as marked by arrows in Fig. 3C. The inset shows the derivative of the data highlighting the opposite slopes of the two transients. Moreover, the obtained DoEI initially decreases slowly and rapidly drops and becomes negative. At t = 4.5 ns, the electrons have completed the full cycloid and the DoEI reaches its global minimum. Last, at $t = T_{SAW}$ = 5.15 ns, the next cycle starts with the quench of the emission of QW2 and DoEI increases again. The local maxima of DoEI may arise from a weak but finite motion of the lower mobility holes (*32*, *44*). Together, all observed anticorrelated intensity modulations are faithfully reproducing the cycloidal motion of electrons driven by the transverse electrical spin of the SAW.

DISCUSSION

In summary, the three-dimensional nature of the tubular QW enabled us to faithfully detect electron cycloids driven by the transverse spin momentum of a SAW. Our sensor's ultrafast, subnanosecond temporal resolution is particularly capable of detecting the orientation and, thus, gyration of the electric field vector at frequencies >100 MHz, which are important for phonon-based hybrid quantum technologies (*45*–*51*). Last, our NW-based method paves the way for the direct observation of photonic skyrmions and, eventually, spatially resolved angular momentum detection of light and sound in quantum optical, photonic, and optomechanical systems (*52*–*55*).

MATERIALS AND METHODS

Sample design

IDTs with a design wavelength of λ_{SAW} = 18 μm were patterned directly on oxygen-reduced *Y*-cut $LiNbO_{3-x}$ substrates by electron

beam lithography in a standard lift-off process using a metallization of 10-nm Ti followed by 60-nm Al.

The studied NW is identical to NW5 in our previous publication (*33*) and was grown by molecular beam epitaxy (*56*). It is approximately $l_{NW} = 10$ μm long and contains a hexagonal GaAs core with a diameter of about 60 nm, which is grown along the {111} direction. In the radial direction, the heterostructure was grown around the hexagonal {110} NW sidewall surfaces of the core as shown schematically in fig. S2A. It is built up from 30-nm $Al_{0.3}Ga_{0.7}As$ shell layer followed by a nominally 5-nm-thick radial GaAs QW and a 70-nm-thick $Al_{0.3}Ga_{0.7}As$ second shell layer, resulting in a tubular GaAs QW embedded between two $Al_{0.3}Ga_{0.7}As$ barriers. For passivation, the multishell structure was overgrown by a 5-nm-thin GaAs capping layer.

Phase-locked acousto-optoelectric spectroscopy

Optical measurements reported in this paper were performed in a helium-flow cryostat equipped with integrated rf connectors at temperatures of $T = 8$ K. The NW was excited by an externally triggered diode laser, emitting $\tau_{Laser} = 90$-ps-long pulses at a wavelength of $\lambda_{Laser} = 660$ nm, which was focused to a spot size of $d_{Laser} = 1.5$ μm by a 50× microscope objective. The repetition rate of the laser pulses is actively locked to a well-defined phase of the rf signal generating the SAW. By setting the delay time τ between the laser and the SAW excitation from 0 to T_{SAW}, charge carriers can be excited at a distinct phase of the SAW. The individual emission bands were filtered using a 0.75-m imaging grating monochromator and detected in the time domain using a Si single photon-counting detector. The time resolution of these detectors is $\tau_{SPAD} \leq 350$ ps. Decay times are obtained directly from the raw data without further deconvolution of an instrument response function. Further details on phase-locked acousto-optical spectroscopy can be found in (*32*) and (*57*). Thus, the hierarchy of the system's parameters is $\tau_{Laser} < \tau_{SPAD} < d_{Laser}/c_{SAW} \approx 430$ ps $< d_{axial}/c_{SAW} \approx 570$ ps. Thus, the resolution is ultimately limited in our specific setup by the spatial separation d_{axial} of the two localization regions.

SUPPLEMENTARY MATERIALS

Supplementary material for this article is available at http://advances.sciencemag.org/cgi/content/full/7/31/eabf7414/DC1

REFERENCES AND NOTES

1. L. Rayleigh, On waves propagated along the plane surface of an elastic solid. *Proc. Lond. Math. Soc.* **s1-17**, 4–11 (1885).
2. P. Lodahl, S. Mahmoodian, S. Stobbe, A. Rauschenbeutel, P. Schneeweiss, J. Volz, H. Pichler, P. Zoller, Chiral quantum optics. *Nature* **541**, 473–480 (2017).
3. F. J. Rodriguez-Fortuno, G. Marino, P. Ginzburg, D. O'Connor, A. Martinez, G. A. Wurtz, A. V. Zayats, Near-field interference for the unidirectional excitation of electromagnetic guided modes. *Science* **340**, 328–330 (2013).
4. J. Petersen, J. Volz, A. Rauschenbeutel, Chiral nanophotonic waveguide interface based on spin-orbit interaction of light. *Science* **346**, 67–71 (2014).
5. A. Aiello, P. Banzer, M. Neugebauer, G. Leuchs, From transverse angular momentum to photonic wheels. *Nat. Photonics* **9**, 789–795 (2015).
6. K. Y. Bliokh, F. Nori, Transverse spin of a surface polariton. *Phys. Rev. A* **85**, 061801 (2012).
7. K. Y. Bliokh, A. Y. Bekshaev, F. Nori, Extraordinary momentum and spin in evanescent waves. *Nat. Commun.* **5**, 3300 (2014).
8. K. Y. Bliokh, D. Smirnova, F. Nori, Quantum spin Hall effect of light. *Science* **348**, 1448–1451 (2015).
9. T. van Mechelen, Z. Jacob, Universal spin-momentum locking of evanescent waves. *Optica* **3**, 118 (2016).
10. F. Khosravi, C. L. Cortes, Z. Jacob, Spin photonics in 3D whispering gallery mode resonators. *Opt. Express* **27**, 15846–15855 (2019).
11. L. Peng, L. Duan, K. Wang, F. Gao, L. Zhang, G. Wang, Y. Yang, H. Chen, S. Zhang, Transverse photon spin of bulk electromagnetic waves in bianisotropic media. *Nat. Photonics* **13**, 878–882 (2019).
12. C. H. Li, O. M. J. van't Erve, J. T. Robinson, Y. Liu, L. Li, B. T. Jonker, Electrical detection of charge-current–induced spin polarization due to spin-momentum locking in Bi_2Se_3. *Nat. Nanotechnol.* **9**, 218–224 (2014).
13. S. Wu, V. Fatemi, Q. D. Gibson, K. Watanabe, T. Taniguchi, R. J. Cava, P. Jarillo-Herrero, Observation of the quantum spin Hall effect up to 100 Kelvin in a monolayer crystal. *Science* **359**, 76–79 (2018).
14. Y. Shi, J. Kahn, B. Niu, Z. Fei, B. Sun, X. Cai, B. A. Francisco, D. Wu, Z.-X. Shen, X. Xu, D. H. Cobden, Y.-T. Cui, Imaging quantum spin Hall edges in monolayer WTe 2. *Sci. Adv.* **5**, eaat8799 (2019).
15. I. Söllner, S. Mahmoodian, S. L. Hansen, L. Midolo, A. Javadi, G. Kiršanskė, T. Pregnolato, H. El-Ella, E. H. Lee, J. D. Song, S. Stobbe, P. Lodahl, Deterministic photon-emitter coupling in chiral photonic circuits. *Nat. Nanotechnol.* **10**, 775–778 (2015).
16. S. Barik, A. Karasahin, C. Flower, T. Cai, H. Miyake, W. DeGottardi, M. Hafezi, E. Waks, A topological quantum optics interface. *Science* **359**, 666–668 (2018).
17. T. Ozawa, H. M. Price, A. Amo, N. Goldman, M. Hafezi, L. Lu, M. C. Rechtsman, D. Schuster, J. Simon, O. Zilberberg, I. Carusotto, Topological photonics. *Rev. Mod. Phys.* **91**, 015006 (2019).
18. J. Lin, J. P. B. Mueller, Q. Wang, G. Yuan, N. Antoniou, X.-C. Yuan, F. Capasso, Polarization-controlled tunable directional coupling of surface plasmon polaritons. *Science* **340**, 331–334 (2013).
19. S.-H. Gong, F. Alpeggiani, B. Sciacca, E. C. Garnett, L. Kuipers, Nanoscale chiral valley-photon interface through optical spin-orbit coupling. *Science* **359**, 443–447 (2018).
20. A. Osada, R. Hisatomi, A. Noguchi, Y. Tabuchi, R. Yamazaki, K. Usami, M. Sadgrove, R. Yalla, M. Nomura, Y. Nakamura, Cavity optomagnonics with spin-orbit coupled photons. *Phys. Rev. Lett.* **116**, 223601 (2016).
21. B. Gohler, V. Hamelbeck, T. Z. Markus, M. Kettner, G. F. Hanne, Z. Vager, R. Naaman, H. Zacharias, Spin selectivity in electron transmission through self-assembled monolayers of double-stranded DNA. *Science* **331**, 894–897 (2011).
22. R. Naaman, Y. Paltiel, D. H. Waldeck, Chiral molecules and the electron spin. *Nat. Rev. Chem.* **3**, 250–260 (2019).
23. Y. Long, J. Ren, H. Chen, Intrinsic spin of elastic waves. *Proc. Natl. Acad. Sci. U.S.A.* **115**, 9951–9955 (2018).
24. K. Y. Bliokh, F. Nori, Spin and orbital angular momenta of acoustic beams. *Phys. Rev. B* **99**, 174310 (2019).
25. L. Burns, K. Y. Bliokh, F. Nori, J. Dressel, Acoustic versus electromagnetic field theory: Scalar, vector, spinor representations and the emergence of acoustic spin. *New J. Phys.* **22**, 053050 (2020).
26. F. J. R. Schülein, E. Zallo, P. Atkinson, O. G. Schmidt, R. Trotta, A. Rastelli, A. Wixforth, H. J. Krenner, Fourier synthesis of radiofrequency nanomechanical pulses with different shapes. *Nat. Nanotechnol.* **10**, 512–516 (2015).
27. P. Delsing, A. N. Cleland, M. J. A. Schuetz, J. Knörzer, G. Giedke, J. I. Cirac, K. Srinivasan, M. Wu, K. C. Balram, C. Bäuerle, T. Meunier, C. J. B. Ford, P. V. Santos, E. Cerda-Méndez, H. Wang, H. J. Krenner, E. D. S. Nysten, M. Weiß, G. R. Nash, L. Thevenard, C. Gourdon, P. Rovillain, M. Marangolo, J.-Y. Duquesne, G. Fischerauer, W. Ruile, A. Reiner, B. Paschke, D. Denysenko, D. Volkmer, A. Wixforth, H. Bruus, M. Wiklund, J. Reboud, J. M. Cooper, Y. Fu, M. S. Brugger, F. Rehfeldt, C. Westerhausen, The 2019 surface acoustic waves roadmap. *J. Phys. D. Appl. Phys.* **52**, 353001 (2019).
28. C. Shi, R. Zhao, Y. Long, S. Yang, Y. Wang, H. Chen, J. Ren, X. Zhang, Observation of acoustic spin. *Natl. Sci. Rev.* **6**, 707–712 (2019).
29. Y. Long, D. Zhang, C. Yang, J. Ge, H. Chen, J. Ren, Realization of acoustic spin transport in metasurface waveguides. *Nat. Commun.* **11**, 4716 (2020).
30. K. A. Ingebrigtsen, Surface waves in piezoelectrics. *J. Appl. Phys.* **40**, 2681–2686 (1969).
31. D. Royer, E. Dieulesaint, *Elastic Waves in Solids I: Free and Guided Propagation* (Springer, 2000).
32. J. B. Kinzel, F. J. R. Schülein, M. Weiß, L. Janker, D. D. Bühler, M. Heigl, D. Rudolph, S. Morkötter, M. Döblinger, M. Bichler, G. Abstreiter, J. J. Finley, A. Wixforth, G. Koblmüller, H. J. Krenner, The native material limit of electron and hole mobilities in semiconductor nanowires. *ACS Nano* **10**, 4942–4953 (2016).
33. M. M. Sonner, A. Sitek, L. Janker, D. Rudolph, D. Ruhstorfer, M. Döblinger, A. Manolescu, G. Abstreiter, J. J. Finley, A. Wixforth, G. Koblmüller, H. J. Krenner, Breakdown of corner states and carrier localization by monolayer fluctuations in radial nanowire quantum wells. *Nano Lett.* **19**, 3336–3343 (2019).
34. R. S. Weis, T. K. Gaylord, Lithium niobate: Summary of physical properties and crystal structure. *Appl. Phys. A* **37**, 191–203 (1985).
35. L. Shao, M. Yu, S. Maity, N. Sinclair, L. Zheng, C. Chia, A. Shams-Ansari, C. Wang, M. Zhang, K. Lai, M. Lončar, Microwave-to-optical conversion using lithium niobate thin-film acoustic resonators. *Optica* **6**, 1498 (2019).
36. W. Jiang, R. N. Patel, F. M. Mayor, T. P. McKenna, P. Arrangoiz-Arriola, C. J. Sarabalis, J. D. Witmer, R. van Laer, A. H. Safavi-Naeini, Lithium niobate piezo-optomechanical crystals. *Optica* **6**, 845 (2019).

37. E. D. S. Nysten, A. Rastelli, H. J. Krenner, A hybrid (Al)GaAs-$LiNbO_3$ surface acoustic wave resonator for cavity quantum dot optomechanics. *Appl. Phys. Lett.* **117**, 121106 (2020).
38. M. J. A. Schuetz, J. Knörzer, G. Giedke, L. M. K. Vandersypen, M. D. Lukin, J. I. Cirac, Acoustic traps and lattices for electrons in semiconductors. *Phys. Rev. X* **7**, 041019 (2017).
39. S. M. Barnett, L. Allen, Orbital angular momentum and nonparaxial light beams. *Opt. Commun.* **110**, 670–678 (1994).
40. M. F. Picardi, A. V. Zayats, F. J. Rodríguez-Fortuño, Janus and huygens dipoles: Near-field directionality beyond spin-momentum locking. *Phys. Rev. Lett.* **120**, 117402 (2018).
41. M. F. Picardi, K. Y. Bliokh, F. J. Rodríguez-Fortuño, F. Alpeggiani, F. Nori, Angular momenta, helicity, and other properties of dielectric-fiber and metallic-wire modes. *Optica* **5**, 1016 (2018).
42. M. Weiß, J. B. Kinzel, F. J. R. Schülein, M. Heigl, D. Rudolph, S. Morkötter, M. Döblinger, M. Bichler, G. Abstreiter, J. J. Finley, G. Koblmüller, A. Wixforth, H. J. Krenner, Dynamic acoustic control of individual optically active quantum dot-like emission centers in heterostructure nanowires. *Nano Lett.* **14**, 2256–2264 (2014).
43. J. S. Blakemore, Semiconducting and other major properties of gallium arsenide. *J. Appl. Phys.* **53**, R123 (1982).
44. A. García-Cristóbal, A. Cantarero, F. Alsina, P. V. Santos, Spatiotemporal carrier dynamics in quantum wells under surface acoustic waves. *Phys. Rev. B* **69**, 205301 (2004).
45. M. J. A. Schuetz, E. M. Kessler, G. Giedke, L. M. K. Vandersypen, M. D. Lukin, J. I. Cirac, Universal quantum transducers based on surface acoustic waves. *Phys. Rev. X* **5**, 031031 (2015).
46. M. V. Gustafsson, T. Aref, A. F. Kockum, M. K. Ekstrom, G. Johansson, P. Delsing, Propagating phonons coupled to an artificial atom. *Science* **346**, 207–211 (2014).
47. S. J. Whiteley, G. Wolfowicz, C. P. Anderson, A. Bourassa, H. Ma, M. Ye, G. Koolstra, K. J. Satzinger, M. V. Holt, F. J. Heremans, A. N. Cleland, D. I. Schuster, G. Galli, D. D. Awschalom, Spin-phonon interactions in silicon carbide addressed by Gaussian acoustics. *Nat. Phys.* **15**, 490–495 (2019).
48. A. Bienfait, K. J. Satzinger, Y. P. Zhong, H.-S. Chang, M.-H. Chou, C. R. Conner, É. Dumur, J. Grebel, G. A. Peairs, R. G. Povey, A. N. Cleland, Phonon-mediated quantum state transfer and remote qubit entanglement. *Science* **364**, 368–371 (2019).
49. M. Weiß, D. Wigger, M. Nägele, K. Müller, J. J. Finley, T. Kuhn, P. Machnikowski, H. J. Krenner, Optomechanical wave mixing by a single quantum dot. *Optica* **8**, 291 (2021).
50. D. A. Golter, T. Oo, M. Amezcua, K. A. Stewart, H. Wang, Optomechanical quantum control of a nitrogen-vacancy center in diamond. *Phys. Rev. Lett.* **116**, 143602 (2016).
51. E. A. Cerda-Méndez, D. N. Krizhanovskii, M. Wouters, R. Bradley, K. Biermann, K. Guda, R. Hey, P. V. Santos, D. Sarkar, M. S. Skolnick, Polariton condensation in dynamic acoustic lattices. *Phys. Rev. Lett.* **105**, 116402 (2010).
52. T. van Mechelen, Z. Jacob, Photonic Dirac monopoles and skyrmions: Spin-1 quantization [Invited]. *Opt. Mater. Exp.* **9**, 95 (2019).
53. V. Peano, C. Brendel, M. Schmidt, F. Marquardt, Topological phases of sound and light. *Phys. Rev. X* **5**, 031011 (2015).
54. C. Brendel, V. Peano, O. Painter, F. Marquardt, Snowflake phononic topological insulator at the nanoscale. *Phys. Rev. B* **97**, 020102 (2018).
55. M. Forsch, R. Stockill, A. Wallucks, I. Marinković, C. Gärtner, R. A. Norte, F. van Otten, A. Fiore, K. Srinivasan, S. Gröblacher, Microwave-to-optics conversion using a mechanical oscillator in its quantum ground state. *Nat. Phys.* **16**, 69–74 (2020).
56. D. Rudolph, S. Funk, M. Döblinger, S. Morkötter, S. Hertenberger, L. Schweickert, J. Becker, S. Matich, M. Bichler, D. Spirkoska, I. Zardo, J. J. Finley, G. Abstreiter, G. Koblmüller, Spontaneous alloy composition ordering in GaAs-AlGaAs core–shell nanowires. *Nano Lett.* **13**, 1522–1527 (2013).
57. M. Weiß, H. J. Krenner, Interfacing quantum emitters with propagating surface acoustic waves. *J. Phys. D. Appl. Phys.* **51**, 373001 (2018).
58. G. Gautschi, *Piezoelectric Sensorics* (Springer, 2002).

Acknowledgments: We thank A. Wixforth for enlightening discussion and continuous support. **Funding:** This work was supported by the Deutsche Forschungsgemeinschaft (DFG) via the Research grants KR3790/6-1 and KO4005/6-1, the Excellence Initiative of the German Federal Government via the Cluster of Excellence Nanosystems Initiative Munich (NIM), and DARPA Nascent Light-Matter Interactions program. **Author contributions:** H.J.K. and Z.J. conceived the idea and supervised the work. D.R. and G.K. performed crystal growth and characterization of NW. L.J. fabricated the SAW chip. M.M.S. and L.J. conducted experiments. F.K. performed numerical calculations of the transverse spin momentum. M.M.S., F.K., Z.J., and H.J.K. analyzed data and wrote the manuscript. **Competing interests:** The authors declare that they have no competing interests. **Data and materials availability:** All data needed to evaluate the conclusions in the paper are present in the paper and/or the Supplementary Materials.

Submitted 16 November 2020
Accepted 11 June 2021
Published 28 July 2021
10.1126/sciadv.abf7414

Citation: M. M. Sonner, F. Khosravi, L. Janker, D. Rudolph, G. Koblmüller, Z. Jacob, H. J. Krenner, Ultrafast electron cycloids driven by the transverse spin of a surface acoustic wave. *Sci. Adv.* **7**, eabf7414 (2021).

Ultrafast electron cycloids driven by the transverse spin of a surface acoustic wave

Maximilian M. Sonner, Farhad Khosravi, Lisa Janker, Daniel Rudolph, Gregor Koblmüller, Zubin Jacob and Hubert J. Krenner

Sci Adv **7** (31), eabf7414.
DOI: 10.1126/sciadv.abf7414